

Generation of time-independent torque by ultrasonic guided waves

I.A. Nedospasov^a, P.D. Pupyrev^b, A. Sotnikov^c, H. Schmidt^c, M. Weihnacht^d, A.P. Mayer^{b,*}

^a Kotelnikov Institute of Radio Engineering and Electronics, Russian Academy of Sciences, Mokhovaya str. 11-7 125009, Moscow, Russia

^b HS Offenburg – University of Applied Sciences, Klosterstr. 14 77723, Gengenbach, Germany

^c Leibniz Institute for Solid State and Materials Research, Helmholtzstraße 20 01069, Dresden, Germany

^d INNOXACS – Innovations in Crystal Acoustics, Am Muehlfeld 34 01744, Dippoldiswalde, Germany

ARTICLE INFO

Keywords:

Guided waves
Angular momentum
Surface acoustic waves
Finite element method

ABSTRACT

The excitation of acoustic waves by a unidirectional transducer, integrated in a piezoelectric cylindrical tube or disk, can lead to a time-independent torque. This phenomenon, demonstrated earlier in experiments and analyzed with coupling-of mode theory, is explained in detail, starting on the level of lattice dynamics of a piezoelectric crystal. Expressions are derived for the stationary torque in the form of integrals over the volume or surface of the piezoelectric, involving the electric potential and displacement field associated with the acoustic waves generated by the transducer.

Simulations have been carried out with the help of the finite element method for a tube made of PZT for two cases: A pre-defined potential on the surface of the tube and metal electrodes buried in the piezoelectric. The displacement field and electric potential of the high-frequency acoustic waves (between 200 and 300 kHz) were computed and used in the evaluation of the integrals. The attenuation due to various loss channels of the acoustic waves in the system has been analyzed in detail, as this plays a crucial role for the efficiency of torque generation. It is conjectured that time-reversal symmetry, present in the absence of attenuation, prohibits the generation of a static torque at least in the linear limit.

A qualitative comparison is made between the simulations and earlier experiments. Discrepancies are attributed to lack of knowledge of the relevant material constants of the piezoelectric and to a simplified modeling of the electrode geometry in the cylindrical tube, which was necessary for reasons of numerical accuracy.

1. Introduction

Acoustic waves at ultrasound frequencies are used to move and orientate solid objects (acoustophoresis and acoustic rotation and levitation) since a number of years with regard to various practical applications. Ultrasonic motors, for example, based on guided acoustic waves in piezoelectric media, are widespread in optical camera systems [1,2]. An effect which has potential applications in this context was recently reported by the authors of [3–7]. They demonstrated by experiments the rotation of a macroscopic cylindrical tube [3,4,6] and macroscopic disk [7] generated by high-frequency acoustic waves propagating circumferentially along the surface. The latter were excited by a unidirectional interdigital transducer (UIDT). It was shown that for a fixed voltage amplitude between the transducer electrodes, a static (i.e. time-constant) torque was generated that acted on the tube.

So far, a first and preliminary explanation was given on the basis of

the phenomenological COM theory [5]. By an analogy with electromagnetic radiation, it was argued that a force results from the two counter-propagating guided acoustic waves with unequal amplitudes, acting tangentially to the cylinder and being proportional to the net power flow through a plane of the cylinder or tube containing the axis of the cylinder [5,4]. A complete explanation of the effect is still missing.

The main goal of this contribution is to provide a comprehensive derivation of the time-independent torque which arises due to the generation of high-frequency (several hundred kHz) guided acoustic waves by a UIDT on the surface of the tube. A two-dimensional finite element (FE) model is set up for the tube with a unidirectional interdigital transducer. Quantitative results for the time-independent torque are presented which were obtained with the help of the FE method (FEM). The model can be extended in a straightforward way to modified geometries and other types of guided acoustic waves.

The paper is organized in the following way. In the next section, the

* Corresponding author.

E-mail address: andreas.mayer@hs-offenburg.de (A.P. Mayer).

<https://doi.org/10.1016/j.ultras.2024.107250>

Received 24 August 2023; Received in revised form 13 December 2023; Accepted 15 January 2024

Available online 24 January 2024

0041-624X/© 2024 The Author(s). Published by Elsevier B.V. This is an open access article under the CC BY license (<http://creativecommons.org/licenses/by/4.0/>).

system we are considering is introduced in some detail, and the main experimental results of [3,4,6] are summarized.

Section 3 contains the derivation of expressions for the static torque generated by (i) an idealized mechanical transducer which exerts a high-frequency traction on the tube's surface and (ii) by an electrical transducer (e.g. an interdigital transducer (IDT)) which generates a high-frequency electrical field. Both transducers are parts of the tube.

Section 4 shows how the expression for the torque, derived for the case of an electrical transducer in the previous section, is evaluated in FEM calculations pertaining to a tube (system (ii) in Section 3). Special attention is paid to the estimation of the intrinsic damping of the high-frequency acoustic waves since this plays a crucial role for the effect of time-constant torque generation.

This role will be addressed in Section 5, where the results of our FEM calculations are presented. In the conclusion section, a practical application of the investigated effect to the orientation of a body in space is suggested.

2. System

In [3–6], a tube, made of radially poled PZT, was considered, which was suspended at a fixed support by a thread. It had an inner (outer) radius $R_1 = 20$ mm ($R_2 = 22$ mm) and a height of $H = 25$ mm (Fig. 1). On its outer surface, a UIDT was mounted and connected by wires to an external ac voltage source with frequencies between 200 and 300 kHz. The UIDT consists of 10 pairs of electrodes, periodically placed on the tube's surface. It generates guided acoustic waves in the piezoelectric tube. These may be regarded as counter-propagating circumferential waves with different amplitudes in the two opposite directions.

The essential experimental findings were the following: After the voltage source was switched on, the tube started to rotate around its axis. The thread, together with the wires connecting the UIDT with the voltage source, constitute an effective torsional spring for the rotating tube with an effective torsion spring constant K . Therefore, the tube carried out damped torsional vibrations and eventually came to rest. Its rest position was not its initial position, but the rotation angle θ reached a non-zero static value θ_s . The finite static torsion angle θ_s corresponds to a time-constant torque $M = K \theta_s$. This static torque was found to be proportional to the square of the input voltage.

3. Theory of torque generation

The following derivations and notation partly follow reasoning and notation in the textbook by Nelson [8]. These derivations are kept sufficiently general such that they can also be used to describe nonlinear

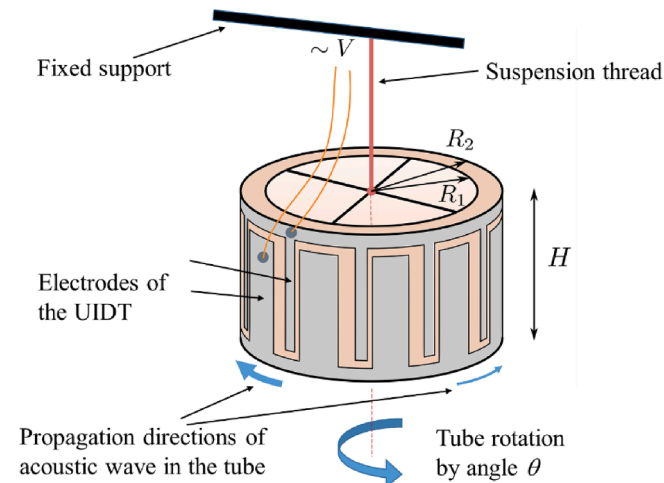


Fig. 1. Schematic drawing of tube with unidirectional transducer.

effects that may occur at high excitation power.

3.1. Torque generated by an “idealized mechanical transducer”

In the first part of this section, we consider a tube or cylinder with circular cross section, which has an “idealized mechanical transducer” on its outer surface. This transducer generates a time-harmonic traction

$$\tau_n(\mathbf{X}, t) = \tilde{\tau}_n(\mathbf{X})e^{i\omega t} + c.c. \quad (1)$$

on the surface, $\mathbf{X} \in \partial V$, where ∂V is the surface of the spatial area V of the tube that contains material. The imaginary unit is denoted by i , ω stands for the angular frequency, and $c.c.$ for the complex conjugate of the preceding term. Here and in the sequel of this paper, lower-case Latin indices refer to the Cartesian spatial frame, upper-case Latin indices to the Cartesian material frame. X_I denotes the I -th component of the position vector \mathbf{X} of a mass element in the undeformed medium, referring to the material frame. Summation over repeated Cartesian indices is implied.

In the linear approximation, the traction (1) generates a displacement field

$$u_n(\mathbf{X}, t) = \tilde{u}_n(\mathbf{X})e^{i\omega t} + c.c. \quad (2)$$

for $\mathbf{X} \in V$. Nonlinearity leads to higher harmonics and usually also to a static part of the displacement field.

The torque $M^{(m)}$ exerted on the tube by the transducer has Cartesian components

$$M_l^{(m)}(t) = \epsilon_{lmn} \int_{\partial V} [X_J \delta_{Jm} + u_m(\mathbf{X}, t)] \tau_n(\mathbf{X}, t) dA \quad (3)$$

where (ϵ_{lmn}) is the Levi-Civita symbol and dA is the scalar surface element in the material frame. The time dependence of M_l is of the form

$$M_l^{(m)}(t) = M_l^{(+)} e^{i\omega t} + M_l^{(-)} e^{-i\omega t} + M_l^{(0)} + (\text{higher harmonics}) \quad (4)$$

Neglecting terms of third and higher order of the traction $\tilde{\tau}$, which occur as nonlinear response of the elastic media, the time-independent amplitudes are given by

$$M_l^{(+)} = \epsilon_{lmn} \int_{\partial V} X_J \delta_{Jm} \tilde{\tau}_n(\mathbf{X}) dA = M_l^{(-)*} \quad (5)$$

$$M_l^{(0)} = \epsilon_{lmn} \int_{\partial V} \tilde{u}_m^*(\mathbf{X}) \tilde{\tau}_n(\mathbf{X}) dA + c.c. \quad (6)$$

With the help of Green's theorem, the surface integral may be converted into volume integrals in the following way, introducing the first Piola-Kirchhoff stress tensor \mathbf{T} :

$$\begin{aligned} \epsilon_{lmn} \int_V [X_J \delta_{Jm} + u_m(\mathbf{X}, t)] \frac{\partial}{\partial X_K} T_{nK}(\mathbf{X}, t) dV &= \\ = \epsilon_{lmn} \int_{\partial V} [X_J \delta_{Jm} + u_m(\mathbf{X}, t)] T_{nK}(\mathbf{X}, t) dA_K & \\ - \epsilon_{lmn} \int_V \left[\delta_{Km} + \left(\frac{\partial}{\partial X_K} u_m(\mathbf{X}, t) \right) \right] T_{nK}(\mathbf{X}, t) dV & \end{aligned} \quad (7)$$

Here, dV is the volume element and dA_K the K -component of the vectorial surface element, both referring to the material frame.

Apart from a scalar factor (Jacobi determinant), the integrand in the second term on the right-hand side of (7) is the (mn) -component of the Cauchy stress tensor, which is symmetric. Therefore, this term vanishes. The first term (surface integral) on the right-hand side of (7) is equal to

the right-hand side of (3) plus, possibly, an additional external torque $\mathbf{M}^{(\text{ext})}$ acting on the tube. In our system, this would be the torque resulting from the torsion of the suspension wire, and it would be time-independent once the tube has come to rest. Making use of the equation of motion for the displacement field,

$$\rho(\mathbf{X}) \frac{\partial^2}{\partial t^2} u_n(\mathbf{X}, t) = \frac{\partial}{\partial X_K} T_{nK}(\mathbf{X}, t) \quad (8)$$

with ρ being the mass density of the undeformed medium, and the boundary condition

$$[N_K(\mathbf{X}) T_{nK}(\mathbf{X}, t) - \tau_n(\mathbf{X}, t)]_{X \in \partial V} = 0 \quad (9)$$

at the surface of the tube leads eventually to the relation

$$\begin{aligned} & \frac{\partial}{\partial t} \epsilon_{lmn} \int_V [X_J \delta_{Jm} + u_m(\mathbf{X}, t)] \rho(\mathbf{X}) \frac{\partial}{\partial t} u_n(\mathbf{X}, t) dV \\ &= \epsilon_{lmn} \int_{\partial V} [X_J \delta_{Jm} + u_m(\mathbf{X}, t)] \tau_n(\mathbf{X}, t) dA + M_l^{(\text{ext})} \end{aligned} \quad (10)$$

In (9), N is a unit vector normal to the surface. The left-hand side of (10) is the derivative w.r.t. time of the total mechanical angular momentum associated with acoustic waves in the tube. In a stationary situation, when the tube has come to rest, the static part $L_3^{(\text{static})}$ of the third component of this angular momentum, for example, is

$$L_3^{(\text{static})} = 4\omega \Im \int_V \tilde{u}_1^*(\mathbf{X}) \rho(\mathbf{X}) \tilde{u}_2(\mathbf{X}) dV \quad (11)$$

up to terms of second order in $\tilde{\tau}$. (\Im denotes the imaginary part.) Obviously, it is only the spin part of the angular momentum [9] which is relevant here. The spin associated with acoustic waves has recently attracted new attention (see for example [9] for a very recent publication concerning this topic with references to earlier work).

Since the time derivative of $L^{(\text{static})}$ vanishes, (10) yields in the stationary case

$$M_l^{(0)} = -M_l^{(\text{ext})} \quad (12)$$

3.2. Torque generated by an electrical transducer

With the charges on its electrodes, an electrical transducer generates an electrical field by which it exerts a force and a torque on charged particles of a material. These particles can be the atoms in the unit cells of a piezoelectric crystal. We consider an electrical transducer, which is part of the tube, and assume that the electric field in the tube is not influenced by external charges.

The total torque exerted on the piezoelectric medium by the electrical transducer is thus

$$\mathbf{M}^{(e)}(t) = \sum_{\ell, \kappa} [\mathbf{X}(\ell, \kappa) + \mathbf{u}(\ell, \kappa; t)] \times q_\kappa \mathbf{E}(\mathbf{X}(\ell, \kappa) + \mathbf{u}(\ell, \kappa; t), t) \quad (13)$$

In (13), $\mathbf{X}(\ell, \kappa)$ denotes the static equilibrium position of the atom belonging to sublattice κ in the ℓ -th unit cell of the piezoelectric crystal, $\mathbf{u}(\ell, \kappa; t)$ its displacement from this position, q_κ the charge of atoms belonging to sublattice κ , and $\mathbf{E}(\mathbf{x}, t)$ is the electric field at position \mathbf{x} and time t . The sum runs over all atoms in the crystal.

We now decompose $\mathbf{X}(\ell, \kappa) = \mathbf{X}(\ell) + \mathbf{X}(\kappa)$, where $\mathbf{X}(\ell)$ is the static equilibrium position of the center of mass of the ℓ -th unit cell, and we define $\mathbf{u}^{(\text{CM})}(\ell; t)$ to be the displacement of this center of mass.

One may pass to the continuum limit [8] by replacing $\mathbf{X}(\ell)$ by the continuous variable \mathbf{X} and define the following functions:

$\mathbf{u}^{(\text{CM})}(\mathbf{X}, t)$ being equal to $\mathbf{u}^{(\text{CM})}(\ell; t)$ at $\mathbf{X} = \mathbf{X}(\ell)$ and being identified with the mechanical displacement field $\mathbf{u}(\mathbf{X}, t)$, and

$\mathbf{u}^{(\kappa)}(\mathbf{X}, t)$ being equal to $\mathbf{u}(\ell, \kappa; t)$ at $\mathbf{X} = \mathbf{X}(\ell)$.

Sums over the unit cell label ℓ become volume integrals,

$$\sum_{\ell} \cdots \rightarrow \frac{1}{V_u} \int_V \cdots dV = \frac{1}{V_u} \int_V \cdots \hat{J}(\mathbf{x})^{-1} dv \quad (14)$$

where V_u is the volume of the undeformed unit cell of the crystal, and dV is the volume element in the material frame. Furthermore, v is the volume of the deformed crystal and dv the volume in the spatial frame, $\mathbf{x} = \mathbf{X} + \mathbf{u}(\mathbf{X})$ denotes the position of a mass element in the deformed crystal, referring to the spatial frame, and $\hat{J}(\mathbf{x})$ is the Jacobi determinant for the transition of integration variables $\mathbf{X} \rightarrow \mathbf{x}$.

Assuming charge neutrality of the unit cells, i.e. $\sum_{\kappa} q_{\kappa} = 0$, we obtain for the dipole moment of a unit cell in the continuum limit:

$$\begin{aligned} \sum_{\kappa} q_{\kappa} [\mathbf{X}(\kappa) + \mathbf{u}(\ell, \kappa) - \mathbf{u}^{(\text{CM})}(\ell)] & \rightarrow \sum_{\kappa} q_{\kappa} [\mathbf{X}(\kappa) + \mathbf{u}^{(\kappa)}(\mathbf{X}) - \mathbf{u}(\mathbf{X})] \\ &= \sum_{\kappa} q_{\kappa} [\mathbf{X}(\kappa) + \mathbf{u}^{(\kappa)}(\mathbf{X})] = V_u \hat{J}(\mathbf{x}) \mathbf{P}(\mathbf{x}) \end{aligned} \quad (15)$$

with the polarization vector $\mathbf{P}(\mathbf{x})$.

When passing to the continuum limit on the right-hand side of (13), we first expand $\mathbf{E}(\mathbf{X}(\ell, \kappa) + \mathbf{u}(\ell, \kappa; t), t)$ in powers of the deviations of the spatial argument from $\mathbf{X}(\ell) + \mathbf{u}^{(\text{CM})}(\ell, t)$,

$$\begin{aligned} \mathbf{E}_m(\mathbf{X}(\ell, \kappa) + \mathbf{u}(\ell, \kappa; t), t) &= \mathbf{E}_m(\mathbf{X}(\ell) + \mathbf{u}^{(\text{CM})}(\ell, t), t) \\ &+ [\mathbf{X}_n(\kappa) + \mathbf{u}_n(\ell, \kappa; t) - \mathbf{u}_n^{(\text{CM})}(\ell, t)] \left[\frac{\partial}{\partial z_n} \mathbf{E}_m(\mathbf{z}, t) \right]_{\mathbf{z}=\mathbf{X}(\ell)+\mathbf{u}^{(\text{CM})}(\ell, t)} + \cdots \end{aligned} \quad (16)$$

Inserting this into (13), keeping terms up to 1st order in the small lengths $|\mathbf{X}(\kappa) + \mathbf{u}(\ell, \kappa; t) - \mathbf{u}^{(\text{CM})}(\ell, t)|$ and passing to the continuum limit yields the following expression for the torque:

$$\mathbf{M}_l^{(e)}(t) = \epsilon_{lmn} \int_V \left\{ P_m(\mathbf{x}, t) E_n(\mathbf{x}, t) + x_m \left[\frac{\partial}{\partial x_k} E_n(\mathbf{x}, t) \right] P_k(\mathbf{x}, t) \right\} dv \quad (17)$$

This expression is identical to the second term on the left-hand side of equation (3.13) in [10], where it has been derived in a different way for an electronic-charge continuum coupled to a deformable mechanical continuum which represents a positively charged crystal lattice. (The first term on the left-hand side of equation (3.13) in [10] corresponds to the mechanical torque $\mathbf{M}^{(m)}$, considered in Subsection 3.1 of this work.)

For practical calculations, it is convenient to convert the expression on the right-hand side of (17) to the material frame. This is done in a straightforward way by introducing a scalar potential $\phi(\mathbf{X}, t)$ being a function of the material position \mathbf{X} and time. Also, a material-frame polarization \mathcal{P} is introduced, which is related to the physical polarization vector \mathbf{P} via $P_m = \hat{J}^{-1} (\partial x_m / \partial X_N) \mathcal{P}_N$ [8]. When confining ourselves to terms of second order in the time-dependent quantities, we obtain

$$\mathbf{M}_l^{(e)}(t) = -\epsilon_{lmn} \delta_{Mm} \delta_{Nn} \int_V \left\{ \mathcal{P}_M(\mathbf{X}, t) \left[\frac{\partial}{\partial X_N} \phi(\mathbf{X}, t) \right] + X_M \mathcal{P}_K(\mathbf{X}, t) \left[\frac{\partial^2}{\partial X_K \partial X_N} \phi(\mathbf{X}, t) \right] \right\} dV \quad (18)$$

A time-harmonic potential $\pm\phi_0 e^{i\omega t} + c.c.$ on the electrodes of an interdigital transducer, where ϕ_0 is a constant, leads to an electrostatic potential and a polarization of the form

$$\phi(\mathbf{X}, t) = \tilde{\phi}(\mathbf{X}) e^{i\omega t} + c.c. \quad (19)$$

$$\mathcal{P}(\mathbf{X}, t) = \tilde{\mathcal{P}}(\mathbf{X}) e^{i\omega t} + c.c. \quad (20)$$

at leading order of ϕ_0 . Likewise, the displacement field excited via piezoelectricity is of the form (2).

Inserting (19), (20) into (18), we obtain for the static part $M^{(e,0)}$ of the torque:

$$M_l^{(e,0)} = -\epsilon_{lmn} \delta_{Mm} \delta_{Nn} \int_V \left\{ \tilde{\mathcal{P}}_M^*(\mathbf{X}) \left[\frac{\partial}{\partial X_N} \tilde{\phi}(\mathbf{X}) \right] + X_M \tilde{\mathcal{P}}_M^*(\mathbf{X}) \left[\frac{\partial^2}{\partial X_K \partial X_N} \tilde{\phi}(\mathbf{X}) \right] \right\} dV + c.c. \quad (21)$$

For a piezoelectric material, $\tilde{\mathcal{P}}$ is related to the displacement and potential gradients via

$$\tilde{\mathcal{P}}_M = e_{MJK} \frac{\partial}{\partial X_K} \tilde{u}_j - \epsilon_0 \chi_{MK} \frac{\partial}{\partial X_K} \tilde{\phi} \quad (22)$$

within linear approximation, where e_{MJK} are the piezoelectric constants of the material, χ_{MK} are the components of its electric susceptibility tensor, and ϵ_0 is the vacuum permittivity.

The volume integral on the right-hand side of (21) with (22) can be evaluated numerically once the spatial distribution of the displacement field and electrostatic potential, excited by the electrical transducer, has been determined.

For certain geometries, a simplification can be achieved by introducing the material form of the electric displacement field

$$\mathcal{D}_K = -\epsilon_0 \frac{\partial}{\partial X_K} \phi + \mathcal{P}_K \quad (23)$$

and applying Green's theorem to the second term of the integrand on the right-hand side of (18). In this way, the latter equation can be brought into the form

$$M_l^{(e)} = -\epsilon_{lmn} \delta_{Mm} \delta_{Nn} \left\{ \frac{1}{2} \epsilon_0 \int_V X_M \frac{\partial}{\partial X_N} |\nabla \phi|^2 dV - \int_V X_M \left[\frac{\partial}{\partial X_N} \phi \right] \mathcal{D}_K dA_K + \epsilon_0 \int_V \left[\frac{\partial}{\partial X_N} \phi \right] \left[\frac{\partial}{\partial X_M} \phi \right] dV - \int_V X_M \left[\frac{\partial}{\partial X_N} \phi \right] \left[\frac{\partial}{\partial X_K} \mathcal{D}_K \right] dV \right\} \quad (24)$$

For simplicity, we have suppressed the time and space arguments t, \mathbf{X} in (22)-(24). The last volume integral on the right-hand side of (24) vanishes because of a Maxwell equation, the second-to-last integral does not contribute to the torque because of its symmetry in connection with the Levi-Civita tensor. The surface integral on the right-hand side of (24) has a simple interpretation. At an interface between the piezoelectric and a metal electrode, $-\mathcal{D}_K N_K$ is the charge per unit area at the interface. (N is the unit vector normal to the interface pointing out into the metal.) Therefore, the surface integral in (24) is the torque due to a surface or interface traction generated by the electrostatic force of the surface or interface charges.

Applying again Green's theorem, the first term in the curly bracket of (24) is readily converted into a surface integral and we obtain for the torque

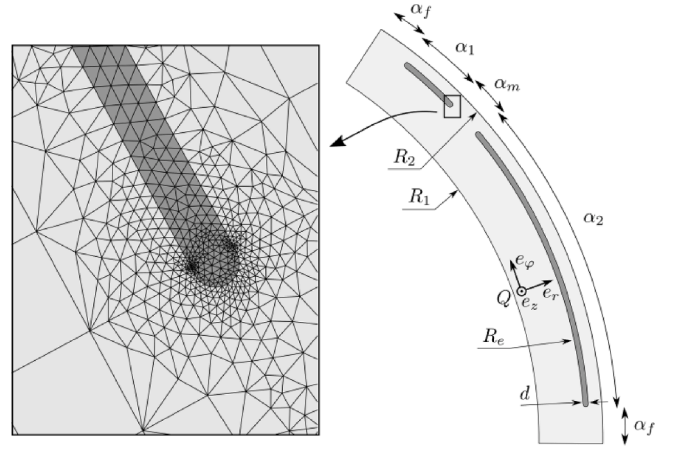


Fig. 2. Right: Unit cell of tube with unidirectional transducer, consisting of two electrodes (dark grey) buried in piezoelectric ceramic (bright grey), local co-ordinate system at an arbitrary material point Q in the tube. Left: mesh pattern for finite element calculations.

$$M_l^{(e)} = -\epsilon_{lmn} \delta_{Mm} \delta_{Nn} \left\{ \int_V X_M \left[\frac{\partial}{\partial X_N} \phi \right] \mathcal{D}_K dA_K + \frac{1}{2} \epsilon_0 \int_V |\nabla \phi|^2 X_M dA_N \right\} \quad (25)$$

A convenient expression for numerical calculations of the torque component $M_3^{(e)}$ in systems with (at least partly) cylindrical symmetry is obtained from (24) after introducing polar coordinates r, φ in the 1–2 plane,

$$M_3^{(e)} = - \int_V \left[\frac{\partial}{\partial \varphi} \phi \right] \mathcal{D}_r dA - \frac{1}{2} \epsilon_0 \int_V \left[\frac{\partial}{\partial \varphi} |\nabla \phi|^2 \right] dV \quad (26)$$

where \mathcal{D}_r is the radial component of the electric displacement field. In the case of a homogeneous tube with prescribed potential on its surfaces, the volume integral in (26) vanishes.

3.3. Excitation by a periodic surface traction or a surface potential

In this subsection we consider two different options for the excitation of acoustic waves in the tube: A mechanical traction at the surface (i) and an electrical potential at the surface of the tube (ii). Both the surface traction and the electrical surface potential have a sinusoidal dependence on time and on the polar angle φ . In addition, we assume that all fields are approximately independent of X_3 . We show for these two cases, that no static torque is generated if no attenuation of the high-frequency acoustic waves is taken into account. We note that the phenomenological COM model invoked in [5] also predicts that attenuation of the acoustic waves is required for the rotation of the tube to occur.

In case (i), the surface traction at $r = R_2$ is of the form

$$\tau_r(\varphi, t) = \hat{\tau}_r e^{i(\omega t - n\varphi)} + c.c. \quad (27a)$$

$$\tau_\varphi(\varphi, t) = i \hat{\tau}_\varphi e^{i(\omega t - n\varphi)} + c.c. \quad (27b)$$

$$\tau_z(\varphi, t) = 0 \quad (27c)$$

where R_2 is the outer radius of the tube (Fig. 1), the indices r, φ, z refer to the local material coordinate system (Fig. 2) associated with cylindrical coordinates r, φ, z , while n is an integer, and $\tilde{\tau}_r, \tilde{\tau}_\varphi$ are real constants. This surface traction generates an acoustic wave with elliptic particle motion similar to Rayleigh waves.

The equation of motion (8) and boundary condition (9) at the surface are conveniently expressed in polar coordinates, together with the constitutive equation for stress and strain. In an isotropic medium without any damping (energy dissipation), it then becomes obvious that a solution for the displacement field can be obtained of the form

$$u_r(r, \varphi, z, t) = \tilde{U}_r(r) e^{i(\omega t - n\varphi)} + c.c. \quad (28a)$$

$$u_\varphi(r, \varphi, z, t) = i\tilde{U}_\varphi(r) e^{i(\omega t - n\varphi)} + c.c. \quad (28b)$$

$$u_z(r, \varphi, z, t) = 0 \quad (28c)$$

in cylindrical coordinates, where $\tilde{U}_r(r), \tilde{U}_\varphi(r)$ are real functions of the radial coordinate r only. This solution is inserted into expression (6) for the time-independent part of the torque along the symmetry axis of the cylinder,

$$M_3^{(0)} = 2\pi H i \left[\tilde{U}_r(R_2) \tilde{\tau}_\varphi + \tilde{U}_\varphi(R_2) \tilde{\tau}_r \right] + c.c. = 0 \quad (29)$$

We assume here that the height H of the tube is sufficiently large in comparison to the radius R_2 such that effects near the top and bottom of the cylindrical tube are negligible.

In case (ii), the high-frequency acoustic waves are excited by an electrical surface potential of the form

$$\phi(R_2, \varphi, z, t) = \hat{\phi} e^{i(\omega t - n\varphi)} + c.c. \quad (30)$$

where $\hat{\phi}$ is a real constant. The procedure in case (i) can be extended to case (ii) by expressing in polar coordinates the equation of motion (8), the mechanical boundary condition (9) in the absence of surface traction, the field equation

$$-\frac{\partial^2}{\partial X_K \partial X_K} \varepsilon_0 \phi(\mathbf{X}, t) + \frac{\partial}{\partial X_K} \mathcal{P}_K(\mathbf{X}, t) = 0 \quad (31)$$

with the electrical boundary conditions (30) at the outer radius and fixed-potential or open-circuit boundary conditions at the inner radius, together with the constitutive equations for a radially poled piezoceramic in the absence of damping. The electrical potential and polarization generated by the imposed surface potential (30) are of the form

$$\phi(r, \varphi, z, t) = \tilde{\phi}(r) e^{i(\omega t - n\varphi)} + c.c. \quad (32a)$$

$$\mathcal{P}_r(r, \varphi, z, t) = \tilde{\mathcal{P}}_r(r) e^{i(\omega t - n\varphi)} + c.c. \quad (32b)$$

$$\mathcal{P}_\varphi(r, \varphi, z, t) = i\tilde{\mathcal{P}}_\varphi(r) e^{i(\omega t - n\varphi)} + c.c. \quad (32c)$$

$$\mathcal{P}_z(r, \varphi, z, t) = 0 \quad (32d)$$

with real functions $\tilde{\phi}(r), \tilde{\mathcal{P}}_r(r), \tilde{\mathcal{P}}_\varphi(r)$ of the radial coordinate r . Transforming the expression on the right-hand side of (21) to polar coordinates and inserting (32), a purely imaginary integrand results and hence the time-independent torque $M_3^{(e,0)}$ vanishes.

Damping due to viscosity in case (i) or due to viscosity and/or dielectric losses in case (ii) introduces additional terms in the equations of motion and boundary conditions which preclude solutions of the form (28) or (32) with only real functions of the radial coordinate.

It is straightforward to extend the proof outlined above to more general forms of the surface traction

$$\tau_r(\varphi, t) = \tilde{\tau}_r(\varphi) e^{i\omega t} + c.c. \quad (33a)$$

$$\tau_\varphi(\varphi, t) = i\tilde{\tau}_\varphi(\varphi) e^{i\omega t} + c.c. \quad (33b)$$

and electrical surface potential

$$\phi(R_2, \varphi, z, t) = \tilde{\phi}(\varphi) e^{i\omega t} + c.c. \quad (34)$$

as long as the electrical surface potential or surface traction with real functions $\tilde{\tau}_r(\varphi), \tilde{\tau}_\varphi(\varphi), \tilde{\phi}(\varphi)$ can be represented as Fourier series. At least formally, this can be done in the case of metal electrodes fixed at the outer surface of a piezoelectric tube, as shown in Appendix A.

4. Numerical calculations

In order to obtain an estimate of the static torque predicted by the expressions (21) or (26) for a macroscopic tube of the dimensions given in [3], finite element models (FEM) have been set up. To keep the numerical effort low, these models are two-dimensional in that the dependence of all fields on the coordinate along the symmetry axis of the tube (3-axis) is neglected. However, the vector fields may have a non-vanishing 3-component.

4.1. Geometry and material constants

A cylindrical tube, made of the radially poled piezo-ceramic PZT-4, has been considered with inner and outer radius R_1, R_2 , respectively. Two ways of electrical excitation were simulated:

- a pre-set potential of the form (30) with $n = 10$ on the outer surface (angular periodicity $\alpha = 36^\circ$, in the following denoted "system (a)") and
- a periodic arrangement of 10 pairs of electrodes with potential $\phi_0 e^{i\omega t} + c.c.$ on one of the two sorts of electrodes with $\phi_0 = 2.5$ V and zero potential on the other (in the following denoted "system (b)"). One of the 10 unit cells of this periodic arrangement is shown in Fig. 2. The electrodes are buried in the PZT. The lengths and angles describing the tube and the position and size of the electrodes are given in Table 1.

For the material of the electrodes we chose isotropic silver with mass density $\rho = 10490$ kg/m³, Young's modulus $E = 8.3 \times 10^{10}$ N/m², and Poisson ratio $\nu = 0.37$. The material constants for PZT-4 used in our calculations are shown below [11].

$$[c] = 10^{10} \begin{bmatrix} 13.9 & 7.78 & 7.43 & 0 & 0 & 0 \\ 7.78 & 13.9 & 7.43 & 0 & 0 & 0 \\ 7.43 & 7.43 & 11.5 & 0 & 0 & 0 \\ 0 & 0 & 0 & 2.56 & 0 & 0 \\ 0 & 0 & 0 & 0 & 2.56 & 0 \\ 0 & 0 & 0 & 0 & 0 & 3.06 \end{bmatrix} \frac{\text{N}}{\text{m}^2} \quad (35a)$$

Table 1
Geometry parameters.

α	36°	R_1	20 mm
α_f	3.3°	R_2	22 mm
α_m	4.5°	R_e	21.79 mm
α_1	4.5°	d	0.02 mm
α_2	20.4°	W	20 mm

$$[e] = \begin{bmatrix} 0 & 0 & 0 & 0 & 12.7 & 0 \\ 0 & 0 & 0 & 12.7 & 0 & 0 \\ -5.2 & -5.2 & 15.1 & 0 & 0 & 0 \end{bmatrix} \frac{\text{C}}{\text{m}^2} \quad (35b)$$

$$[\varepsilon] = \begin{bmatrix} 730 & 0 & 0 \\ 0 & 730 & 0 \\ 0 & 0 & 635 \end{bmatrix} \varepsilon_0 \quad (35c)$$

where $[c]$, $[e]$, $[\varepsilon]$ denote the tensors of elastic constants at constant electric field, piezoelectric and dielectric constants at constant strain, respectively, referring to the crystallographic coordinate system. Note that the poling direction in the crystallographic coordinate system is the 3-direction, whereas it is the radial direction (being the 1-direction for $\varphi = 0$) in the system considered here. ε_0 is the vacuum permittivity. In (35) we have followed the notation of [12]. The density of PZT-4 is 7500 kg/m³. Among the various types of PZT with a wide range of material properties (see e.g. [13]), we chose data for PZT-4 as this variant was considered in [5] in connection with the experimental work.

4.2. Details of FEM computations

Finite element calculations were carried out in the frequency domain to determine the electrostatic potential and mechanical displacement field for a given time-harmonic potential at the outer surface of the tube (a) or on the buried electrodes (b). From these fields, the static torque was determined by computing volume integrals (double integrals), and surface integrals (single integrals) within the two-dimensional FEM models. The FEM models were set up and the computations were performed with the commercial tool COMSOL Multiphysics and in addition, in the case of excitation by a given surface potential (a), with a self-developed FEM tool, working with quadrangular eight-node elements. Perfect agreement was found between the results obtained with the two different tools. For this comparison, quadrangular elements of second order were used.

Due to the 10-fold periodicity with respect to the angle φ , the computations could be confined to one unit cell with periodic boundary conditions applied to the interfaces between the neighboring cells. The surfaces of the tube were considered to be free of mechanical traction. Open-circuit boundary conditions were applied to free surfaces of the piezoelectric. They should be a good approximation because of the large dielectric constants of PZT.

Although the system (a) can be reduced to a one-dimensional problem by eliminating the φ -dependence, we have treated it as a two-dimensional problem in the (r, φ) -plane for test purposes and accuracy checks.

In system (a) the volume integral in (26) vanishes. The static torque $M_3^{(e,0)}$ was computed in two ways: via a surface integral (first term on the right-hand side of (26)) and via a volume integral in (21) with equal accuracy.

For the tube with metal electrodes (system (b)), the static torque was computed with COMSOL via the volume integral (21). A particular challenge to the numerical accuracy is posed by rapid spatial variations of the electrostatic potential because of its second derivative occurring in (21). For this reason, electrodes with rounded corners were considered which are buried in the piezoelectric material. In addition to quadrangular elements with an edge length of the order of 0.05 mm, triangular elements were employed in the narrow area around the electrodes. They allow for a rapid decrease of element size on short length scales. This is demonstrated in Fig. 2, where a cutout of a typical mesh is shown. The edges of the elements in the middle of an electrode had a length of about 0.007 mm and less than 0.002 mm at its rounded corners. In order to reach higher accuracy, only fourth-order elements were used in computations for system (b). In section 5, we refer to this mesh as the “coarse mesh.” When computing the static torque for system

(b) in the limit of small damping of the ultrasonic waves, a refined mesh was used, where the element sizes were, on average, half of those of the coarse mesh.

The calculations were carried out in cylindrical coordinates. An explicit expression for the 3-component of the torque in terms of derivatives of the field components u_r , u_φ , u_z and ϕ with respect to r and φ is given in Appendix B.

For this system, the admittance Y of the electrical transducer was determined by calculating the current I in one of the two electrodes per unit cell by an integral over a surface S surrounding this electrode:

$$I = i\omega W \int_S \tilde{\mathcal{D}}_K dA_K = Y\phi_0 \quad (36)$$

where ϕ_0 is the amplitude of the oscillating voltage between two neighboring electrodes as defined in subsection 4.1, and $\tilde{\mathcal{D}}$ is defined via $\mathcal{D}(X, t) = \tilde{\mathcal{D}}(X)e^{i\omega t} + \text{c.c.}$, W is the aperture of the UIDT, i.e. the length of the electrodes along the symmetry axis of the tube (the 3-axis).

4.3. Estimate of damping

Since the damping of the high-frequency acoustic waves plays an essential role for the generation of a time-independent torque, the following intrinsic damping mechanisms have been investigated by calculating and comparing the corresponding power loss: Thermo-elastic damping (i), viscous damping (ii), dielectric loss (iii) and Ohmic losses (vi) due to the finite conductivity of the electrodes.

In the case of bulk and surface waves in homogeneous media, thermo-elastic and viscous damping cannot be separated by their frequency dependence. With the data on the specific heat, thermal conductivity and thermal expansion of PZT given in [14] and the values for the viscosity of PZT provided in [15], albeit for different types of PZT, one may conclude that in the case of bulk acoustic waves, thermo-elastic attenuation is by several orders of magnitude smaller than viscous damping. Therefore, it will be neglected.

Following [16], the time-averaged power loss P_R due to the electrical resistance in the electrodes is estimated with the assumption that the current in the electrodes has an approximately linear dependence on the z -coordinate. This results in the following expression for P_R :

$$P_R \approx \frac{\rho_{sp} W}{3hb} (Y\phi_0)(Y\phi_0)^* \quad (37)$$

where h and b are height and width of the electrode, respectively, and ρ_{sp} is the specific resistance of the electrode material. For a rough estimate, the bulk value $\rho_{sp} = 1.6 \times 10^{-8} \Omega\text{m}$ for silver was used. Since the admittance Y has an approximately linear dependence on the aperture W , P_R grows with the third power of W . For the spatial dimensions of the electrodes of the UIDT in [3] (lengths h , b , and W), the Ohmic losses in the electrodes are negligible in comparison to the dielectric and viscous attenuation in the piezoelectric.

Viscous attenuation is accounted for by adding the term $\left(\eta_{jkmN} \frac{\partial^2}{\partial t \partial X_N} u_m\right)$ to the first Piola-Kirchhoff stress tensor component T_{jK} . In [15], values for four of the five independent components of the viscosity tensor η are given for the PZT variants Pz24 and Pz34. They differ by more than one order of magnitude between the two PZT variants. The time-averaged power loss due to viscous damping, P_V , has been estimated by computing

$$P_V = \int_V 2\omega^2 \left[\frac{\partial}{\partial X_K} \tilde{u}_j^*(X) \right] \eta_{jkmN} \left[\frac{\partial}{\partial X_N} \tilde{u}_m(X) \right] dV \quad (38)$$

at various frequencies for the system (b) by FEM. For the viscosity tensor, the simplification

$$\eta_{jKmN} \approx \frac{\delta_m}{\omega} C_{jKmN} \quad (39)$$

with the mechanical loss angle δ_m is introduced. (For the loss angles, we use here the approximation $\tan \delta \approx \delta$.)

For crystalline dielectric materials, the viscosity tensor is usually regarded as frequency-independent. This would imply that the values of the viscosities in [15], referring to a frequency of 25 MHz, can be used in the frequency range considered in this work, too, and δ_m would vary linearly with frequency.

Bodé et al. [17] quantify losses of Pz27 by determining imaginary parts of the elastic constants and dielectric constants. Their findings suggest that the imaginary parts of the elastic constants are largely frequency-independent over a wide frequency range. This implies that the viscosity tensor is inversely proportional to the frequency, and that the mechanical loss angle is frequency-independent.

We have computed the power loss P_V with (38) and (39) for both frequency dependencies of the mechanical loss angle. Since data necessary for a quantitative evaluation of the damping in PZT-4 are not available to us, we had to confine ourselves to a rough order-of-magnitude estimate. For this purpose, we used values for the viscosity η_{33} given in [15] (first case, referring to Pz24 and Pz34), and values for the imaginary part of the elastic constant with real part c_{33} , provided in [17,18] (second case, referring to Pz27).

In the first case, $\delta_m = \omega \eta_{33} / c_{33}$, where Voigt indices are used, referring to the crystallographic coordinate system, with the choices $c_{33} = 11.5 \times 10^{10} \text{ N/m}^2$ from (35a) and $\eta_{33} = 1.0 \text{ kg/(ms)}$, $\eta_{33} = 0.03 \text{ kg/(ms)}$ [15]. In the second case, $\delta_m = c_{33}^* / c_{33}$ with $c_{33}^* = 450 \times 10^6 \text{ N/m}^2$ (imaginary part of elastic constant [17,18]) and the value for $c_{33} = 11.5 \times 10^{10} \text{ N/m}^2$ (real part of elastic constant). For the two cases with these sets of parameters, P_V has been computed by FEM from (38) with (39).

The power loss P_D due to dielectric damping has been estimated by computing

$$P_D = \int_V 2\omega \left[\frac{\partial}{\partial X_M} \tilde{\phi}^*(X) \right] \epsilon_{MN}^* \left[\frac{\partial}{\partial X_N} \tilde{\phi}(X) \right] dV \quad (40)$$

where (ϵ_{MN}^*) is the imaginary part, added to the real dielectric tensor (ϵ_{MN}) specified in (35c). We set

$$\epsilon_{MN}^* \approx \delta_e \epsilon_{MN} \quad (41)$$

with a single dielectric loss angle δ_e , which we assume to be independent of frequency. Dielectric loss angles of PZT variants, deduced from published experimental data known to us, range from 0.001 up to values larger than 0.02, but below 0.05 [15,17–21]. (When values for the complex dielectric tensor were given, we applied the definition $\delta_e =$

$\epsilon_{33}^* / \epsilon_{33}$.) From the data in Fig. 12 in [19] we conclude that $\delta_e \approx 0.004$ is a reasonable approximation for PZT-4. With this value, the dielectric loss P_D was computed from (40) with (41). The FEM calculations of P_V and P_D were carried out at frequencies ranging from 70 to 300 kHz for the PZT tube with pre-set potential on its outer surface (system (a) in subsection 4.1).

In the first case (frequency-independent viscosity) the viscous loss P_V was found to be smaller than the dielectric loss P_D by at least one order of magnitude in the whole frequency range. In the second case (frequency-independent imaginary parts of elastic moduli), the viscous loss at the resonance frequencies of the acoustic modes is approximately of the same order of magnitude as the dielectric loss, but not larger. In view of the uncertainty of the material data relevant for the damping and for simplicity, dielectric loss was considered to be the dominant loss channel. In the FEM simulations carried out to investigate the dependence of the static torque on the dielectric loss angle, the viscous damping was neglected.

5. Results and discussion

5.1. Results of simulations

The acoustic modes occurring in the systems (a) (piezoelectric tube with potential (30) on its outer surface) and (b) (piezoelectric tube with buried UIDT) in the frequency range between 70 and 300 kHz manifest themselves in the quantities shown in Fig. 3. In the calculations pertaining to Fig. 3, damping was accounted for with a dielectric loss angle $\delta_e = 9 \times 10^{-4}$ and a mechanical loss angle of $\delta_m = 2.6 \times 10^{-13} \text{ s} \times \omega$.

The admittance of the UIDT is shown for system (b). Three mode pairs appear (near 70, 220 and 290 kHz). The degeneracy of the counterpropagating waves is lifted by the presence of the periodically arranged electrodes. For system (a), the time-averaged magnitude of the displacement at a point on the outer surface is shown as function of frequency in Fig. 3. The mode with frequency near 220 kHz is not excited by the surface potential (30) with $n = 10$.

As expected, the displacement patterns of the modes have the character of acoustic waves in thin plates, since the thickness of the tube is much smaller than its inner and outer radii. Fig. 4 shows the displacements of two eigenmodes of a tube with material constants of PZT-4 and with traction-free and open-circuit boundary conditions at its inner and outer surface ($r = R_1, R_2$). The corresponding eigenfrequencies are $f = 234 \text{ kHz}$ and $f = 297 \text{ kHz}$. The polarization of the lower-frequency mode is mainly radial, while the second mode is predominantly tangentially polarized.

The static torque resulting from the surface potential in system (a) is shown in Fig. 5a as a function of the dielectric loss angle for two different frequencies. For simplicity, viscous damping has been neglected in these

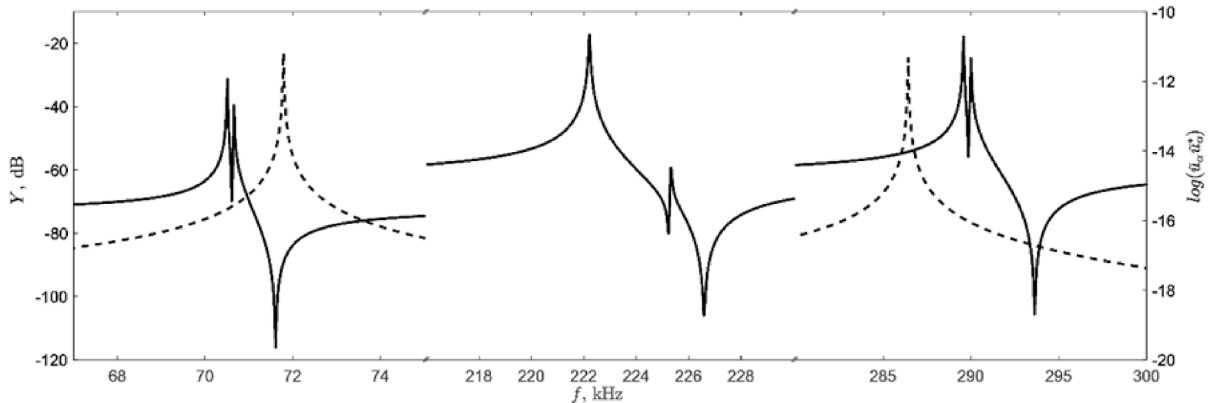


Fig. 3. Frequency response of piezoelectric tube with sinusoidal potential at outer surface (system (a)) or buried electrodes system (b)). Solid: magnitude of admittance for system (b) (left scale). Dashed: Squared magnitude of displacement at one point of outer surface in units of m^2 for system (a) (right scale).

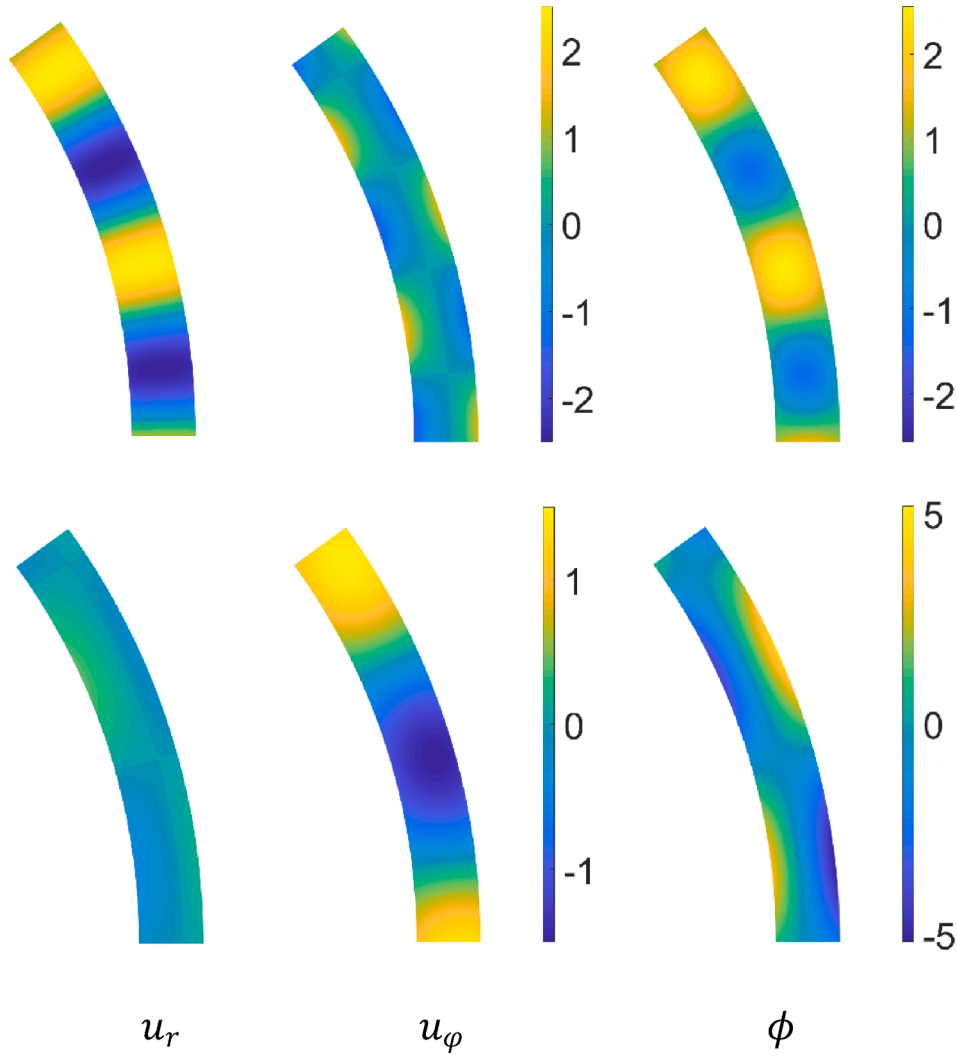


Fig. 4. Displacement patterns of acoustic eigenmodes of the piezoelectric tube with traction free and open-circuit boundary conditions on its surfaces. Upper: Eigenfrequency 234 kHz, $u_r = 1$ nm corresponds to $\phi = 1.105$ V. Lower: Eigenfrequency 297 kHz, $u_\phi = 1$ nm corresponds to $\phi = -0.287$ V.

calculations. In the limit $\delta_e \rightarrow 0$, the torque vanishes, as expected on the basis of the reasoning in subsection 3.3. With increasing δ_e , it passes an extremum. The value of the torque at the extremum as well as its position on the abscissa is strongly frequency-dependent. The latter varies between $\delta_e = 0.01$ and 0.15 for the frequencies considered. This range of δ_e presumably covers the true dielectric loss angle of PZT-4. The results for the torque computed via the surface intergral in (26) and the volume integral in (21) agree very well and are not distinguishable on the scale of Fig. 5a. For completeness, we mention here that for unrealistically large loss angles ($\delta_e > 2$), the static torque would grow linearly with $\tan \delta_e$.

Simulation results for the static torque in system (b) are presented in Fig. 5b. The behavior of this quantity as a function of the dielectric loss angle is qualitatively similar to that of system (a). However, especially near resonance frequencies, high numerical effort is required to achieve reasonable accuracy for the limit $\delta_e \rightarrow 0$, as shown in the inset of Fig. 5b. The results obtained with a refined mesh, defined in Subsection 4.2, (inset of Fig. 5b) that in system (b), the static torque vanishes, too, in the limit $\delta_e \rightarrow 0$.

In Fig. 6a, the dependence of the static torque on the frequency of the counter-propagating acoustic waves is shown for system (b) (piezoelectric tube with buried electrodes). Three different combinations of viscous and dielectric loss parameters were chosen. As already expected on the basis of the findings in [5], the size of the static torque strongly

depends on the attenuation. With decreasing values of the loss parameters, the peak in Fig. 6a contracts and the magnitude of the static torque at the resonance frequency increases. The splitting of the resonance frequency due to the periodic arrangement of electrodes is visible in Fig. 6a only for the case of comparatively small damping (dielectric loss only, with $\delta_e = 0.0037$).

With the assumption that the imaginary part of the elastic moduli of PZT-4 is largely frequency-independent, as claimed in [17], the case $\delta_m = 0.0037$, $\delta_e = 0.0037$ (dashed-dotted lines in Fig. 6) seems to come closest to the experimental situation reported in [3] according to our analysis of the loss mechanisms in PZT. The maximal static torque found experimentally is smaller than the computed maximal magnitude of the static torque by a factor of approximately 200 (Fig. 2 in [3]). The width of the dashed-dotted peak in Fig. 6a is by a factor of about 2 narrower than the corresponding width of the measured curve in [3]. The width of the real part of the computed admittance is also smaller than that of the measured admittance. When doubling the loss parameters δ_e and δ_m , the computed widths come close to the corresponding experimental values for the real part of the admittance and the dependence of the static torque on frequency (solid lines in Fig. 6). However, the maximal magnitude of the computed static torque is still larger than the measured maximum by a factor of around 50.

Likely reasons for the discrepancy between the simulated values for the static torque, presented here, and the measured torque, reported in

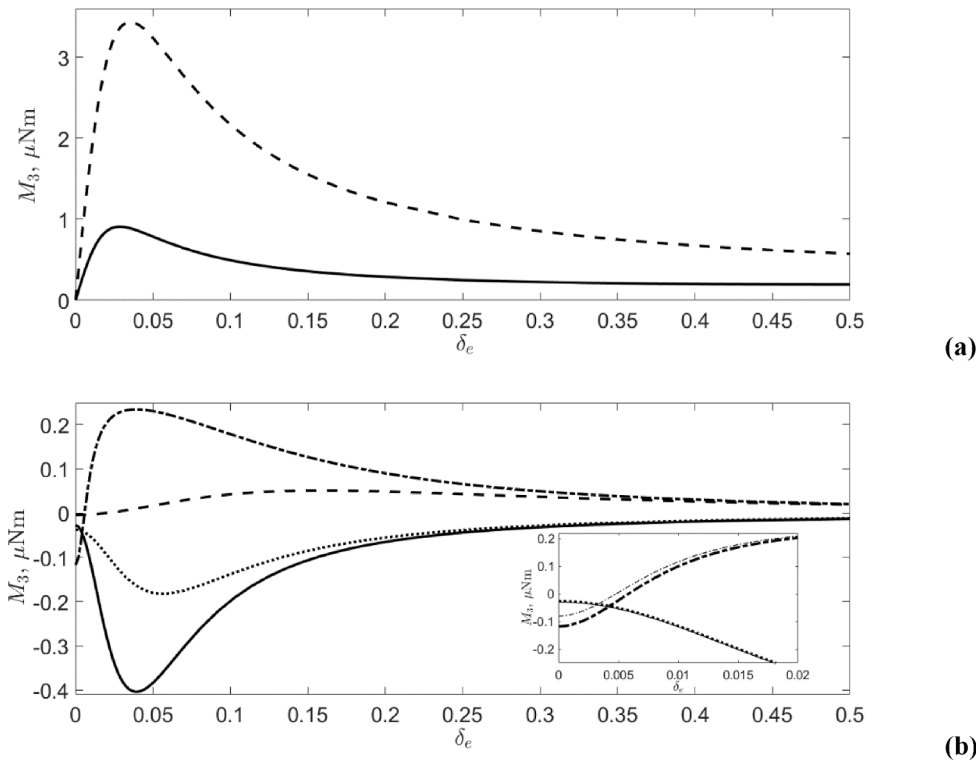


Fig. 5. Dependence of static torque on the dielectric loss angle δ_e . (a): Excitation of acoustic modes in the PZT-4 tube by a sinusoidal potential on the surface (system (a)). 72 kHz (solid), 287 kHz (dashed). (b): Excitation via buried silver electrodes (system (b)). 291 kHz (solid), 289 kHz (dotted), 220 kHz (dashed), 222 kHz (dashed-dotted). Inset: 222 kHz, coarse mesh (thick dashed-dotted), 222 kHz, fine mesh (thin dashed-dotted); 72 kHz, coarse mesh (solid), 72 kHz, fine mesh (dotted).

[3], are the following.

i) The material constants of the PZT, the tube is made of, are poorly known, especially those related to the damping of acoustic waves.

ii) For the simulations, the geometry of the system investigated earlier by experiments, had to be modified. It was reduced to two dimensions, neglecting the dependence of all fields on the coordinate along the symmetry axis of the cylinder. Therefore, contributions from the top and bottom surfaces of the tube, especially from the edges of the electrodes, are not included. It was assumed that this simplification is a good approximation for long and thin tubes. However, the length of the tube considered here is comparable to its inner and outer radii (Table 1). Another notable difference concerns the metal electrodes. In experiments, the electrodes were situated on the outer surface of the cylinder. The rapid variations of the potential near the edges of the electrodes would require extraordinary numerical efforts to reach sufficient accuracy in the volume and surface integrals to be computed for the static torque by FEM. In our simulations, we have therefore buried the electrodes in the PZT. In addition, their edges were rounded to reduce the variations of the field on short length scales.

5.2. Interpretation of the role of damping

Within COM theory and a simplified description based on the power flow associated with surface acoustic waves in an interdigital transducer, it was found in [5] that damping of the acoustic waves is essential for the generation of a static torque. In the absence of damping, the two coupled modes, corresponding to two counter-propagating waves excited by the UIDT, have equal amplitudes.

In this work, we have shown on the level of electro-elasticity theory that the static torque vanishes in the case of a homogeneous piezoelectric tube in the absence of attenuation of the acoustic waves. As a pre-condition, the electrical potential must be presentable as a Fourier series. Our numerical simulations for a UIDT with buried electrodes

suggest that the static torque also vanishes in this case in the limit of zero viscous and dielectric losses.

Invoking an analogous argument used in a plasma-physical context [22], we conjecture that the absence of a static torque in lossless systems is a consequence of time reversal symmetry. Invariance with respect to time reversal means that pre-set potentials with time and angular dependence $\exp[i(\omega t + n\varphi)]$ and $\exp[i(\omega(-t) + n\varphi)]$ generate electric fields, mechanical displacement fields and polarization with the same dependence on the spatial coordinates and hence identical static torque. Since these fields describe waves propagating in opposite directions around the symmetry axis of the tube, this static torque should vanish. Damping breaks the time reversal symmetry. We note that this could also be achieved by a permanent magnet and a magnetostrictive material integrated in the tube.

5.3. Potential applications

The phenomenon of stationary torque generation by high-frequency acoustic modes of a solid object can be applied to controlled rotation and orientation of this object in space. In addition to plate-like modes in a cylindrical tube, corresponding to circumferential waves around the cylinder axis, one may envisage other types of guided acoustic waves like edge or wedge waves [23,24] which can be excited by additional transducers. If a second transducer excites waves localized at the edge of a cylindrical tube and this edge is not vertical to the tube's axis, controlled rotations around an additional axis could be achieved. This way of orientating could be applied to free-standing objects in the absence of gravity or in the presence of buoyancy in liquids. This can be particularly attractive since it was shown that the power needed for exciting the guided acoustic waves in the object can be transferred to it wirelessly [6].

A tube, cylinder or disk brought to rotation by the propagation of guided acoustic waves, constitutes an ultrasonic motor (USM). The most

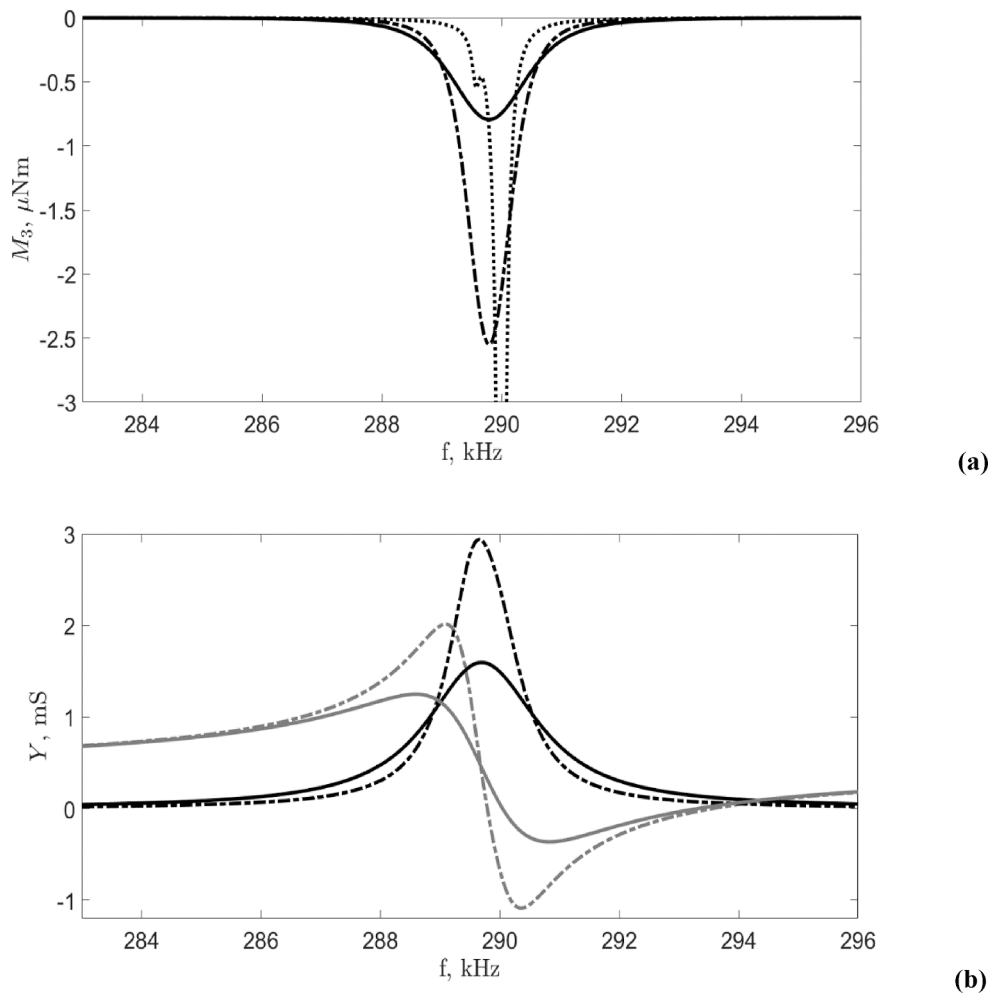


Fig. 6. Frequency dependence of static torque (a) and admittance (b) for dielectric and viscous loss angles $\delta_m = 0.0074, \delta_e = 0.0075$ (solid), $\delta_m = 0.0037, \delta_e = 0.0037$ (dashed-dotted), $\delta_m = 0, \delta_e = 0.0037$ (dotted). Black (grey) lines in (b) correspond to real (imaginary) part of admittance.

widespread USMs work with a stator, where ultrasonic waves are generated. The displacements associated with these waves are coupled to a rotor via friction [1]. This is also the case in USMs with three rotational degrees of freedom with spherically shaped rotors (see [25,26] for recent examples). An ultrasonic motor based on the effect discussed in our study would work without a stator and without friction coupling. It may therefore prove more robust in certain applications.

With wireless power transfer, the effect investigated here may also be used for propulsion, if sufficient angular speed and torque can be achieved. Several tubes or discs could be combined for this purpose.

Detailed investigations, including FEM simulations, are needed to assess the feasibility of these envisaged technical applications. Especially, the system would have to be optimized with regard to increasing the torque.

6. Conclusions

In summary, the phenomenon of the generation of a stationary torque by the excitation of high-frequency acoustic waves in a piezoelectric tube has been traced back to a formula in electro-elasticity theory which has been derived on the basis of lattice dynamics. This formula agrees with the expression derived by Tiersten for an electronic charge continuum coupled to a “lattice continuum” [10]. To evaluate this formula for a tube made of PZT and containing a unidirectional interdigital transducer, finite element calculations have been carried out within a two-dimensional model. The static torque found in these numerical

calculations around the resonance frequency of one of the acoustic modes of the tube strongly exceeds the values measured earlier in a similar system. However, a comparison between measurement and calculations is impeded by the fact that the material constants of the PZT used in the experimental system are not very well known. In addition, the geometry of the simulated system differed to some extent from that of the measured one to keep the numerical effort in reasonable limits.

The theoretical methods employed in this work can also be applied to the simulation of macroscopic disc rotation reported recently in [7]. Especially, they can be used to optimize the geometry of the rotating object to achieve maximal static torque for possible practical applications discussed in the previous section. An extension of the two-dimensional FEM model to three dimensions is straightforward, but requires considerably more numerical resources in order to achieve quantitatively reliable results.

CRedit authorship contribution statement

I.A. Nedospasov: Formal analysis, Funding acquisition, Investigation, Software, Visualization, Writing – original draft. **P.D. Pupyrev:** Formal analysis, Investigation, Software, Validation, Visualization, Writing – review & editing. **A. Sotnikov:** Resources, Writing – review & editing. **H. Schmidt:** Resources, Writing – review & editing. **M. Weinhacht:** Resources, Writing – review & editing. **A.P. Mayer:** Conceptualization, Formal analysis, Investigation, Writing – original draft.

Declaration of competing interest

The authors declare that they have no known competing financial interests or personal relationships that could have appeared to influence the work reported in this paper.

Data availability

Data will be made available on request.

Appendix A

We assume that the potential at the outer surface of the tube is known and can be written as a Fourier series,

$$\phi(R_2, \varphi, t) = e^{i\omega t} \sum_{n=-\infty}^{\infty} \hat{\phi}^{(n)} e^{i\vartheta^{(n)}} e^{-in\varphi} + c.c. \quad (\text{A.1})$$

with real Fourier amplitudes $\hat{\phi}^{(n)}$ and phase angles $\vartheta^{(n)}$. Likewise, we decompose the potential $\phi(r, \varphi, t)$ and the polarization $\mathcal{P}(r, \varphi, t)$ as

$$\phi(r, \varphi, t) = e^{i\omega t} \sum_{n=-\infty}^{\infty} \tilde{\phi}^{(n)}(r) e^{i\vartheta^{(n)}} e^{-in\varphi} + c.c. \quad (\text{A.2})$$

$$\mathcal{P}(r, \varphi, t) = e^{i\omega t} \sum_{n=-\infty}^{\infty} \tilde{\mathcal{P}}^{(n)}(r) e^{i\vartheta^{(n)}} e^{-in\varphi} + c.c. \quad (\text{A.3})$$

where $\tilde{\phi}^{(n)}(r)$ has components $\tilde{\phi}_r^{(n)}(r)$ along the radial and $i\tilde{\phi}_\varphi^{(n)}(r)$ along the tangential direction.

Applying the arguments used in Subsection 3.3 for a surface potential of the form (30) to each Fourier component of (A.1) separately, we conclude that the functions $\tilde{\phi}^{(n)}(r)$, $\tilde{\mathcal{P}}_r^{(n)}(r)$ and $\tilde{\mathcal{P}}_\varphi^{(n)}(r)$ are real in the absence of damping. Inserting the Fourier series (A.2) and (A.3) into the expression on the right-hand side of (21), the phase angles $\vartheta^{(n)}$ drop out from the volume integral, and hence the static torque vanishes.

Appendix B. Evaluation of the static torque in cylindrical coordinates

In cylindrical coordinates, the expression for the 3-component of the static torque on the tube, generated by the electrical transducer, acquires the form

$$M_3^{(e,0)} = W \int_A \epsilon_{3\mu\nu} \left\{ \left(e_{\mu\alpha\beta} \Lambda_{\alpha\beta}^{(1)} - \chi_{\mu\alpha} \Lambda_{\alpha}^{(2)} \right) \Lambda_{\nu}^{(2)*} + r \hat{r}_\mu \Lambda_{\gamma\nu}^{(3)*} \left(e_{\gamma\alpha\beta} \Lambda_{\alpha\beta}^{(1)} - \chi_{\gamma\alpha} \Lambda_{\alpha}^{(2)} \right) \right\} r d\varphi dr + c.c. \quad (\text{B.1})$$

where A is the cross section of the part of the tube filled by the piezo-ceramic, and W is the aperture of the transducer. The Greek indices, running from 1 to 3, refer to the local coordinate system (Fig. 2). Since the PZT in the tube is radially poled, the tensor elements $e_{\gamma\alpha\beta}$ and $\chi_{\mu\alpha}$ are those given in (35) with no rotation. The matrices $\left(\Lambda_{\alpha\beta}^{(1)} \right)$, $\left(\Lambda_{\alpha\beta}^{(3)} \right)$ and the vector $\left(\Lambda_{\alpha}^{(2)} \right)$ depend on the polar coordinates r, φ . Their non-zero components are

$$\Lambda_{11}^{(1)} = \frac{\partial u_r}{\partial r}, \Lambda_{22}^{(1)} = \frac{u_r}{r} + \frac{1}{r} \frac{\partial u_\varphi}{\partial \varphi}, \Lambda_{21}^{(1)} = \frac{1}{r} \frac{\partial u_r}{\partial \varphi} - \frac{u_\varphi}{r}, \Lambda_{12}^{(1)} = \frac{\partial u_\varphi}{\partial r}, \Lambda_{13}^{(1)} = \frac{\partial u_z}{\partial r}, \Lambda_{23}^{(1)} = \frac{1}{r} \frac{\partial u_z}{\partial \varphi} \quad (\text{B.2})$$

$$\Lambda_1^{(2)} = \frac{\partial \phi}{\partial r}, \Lambda_2^{(2)} = \frac{1}{r} \frac{\partial \phi}{\partial \varphi} \quad (\text{B.3})$$

$$\Lambda_{11}^{(3)} = \frac{\partial^2 \phi}{\partial r^2}, \Lambda_{12}^{(3)} = \Lambda_{21}^{(3)} = \frac{1}{r} \frac{\partial^2 \phi}{\partial r \partial \varphi} - \frac{1}{r^2} \frac{\partial \phi}{\partial \varphi}, \Lambda_{22}^{(3)} = \frac{1}{r} \frac{\partial \phi}{\partial r} + \frac{1}{r^2} \frac{\partial \phi}{\partial \varphi} \quad (\text{B.4})$$

References

- [1] C. Zhao, *Ultrasonic motors, technologies and applications*, Springer, Heidelberg, 2011.
- [2] X. Li, Z. Wen, B. Jia, T. Cao, D. Yu, D. Wu, *A review of application and development trends in ultrasonic motors*, *ES Mater. Manuf.* 12 (2021) 3–16.
- [3] S.V. Biryukov, A. Sotnikov, H. Schmidt, Piezoelectric tube rotation effect owing to surface acoustic wave excitation, *Appl. Phys. Lett.* 108 (2016) 134103, <https://doi.org/10.1063/1.4945050>.
- [4] S.V. Biryukov, A. Sotnikov, H. Schmidt, Surface acoustic wave momentum, in *Proc. IEEE Int. Ultrason. Symp. (IUS)*, Tours, France (2016) 1–4.
- [5] S. V. Biryukov, M. Weihnacht, A. Sotnikov, and H. Schmidt, “SAW based rotation force of a cylindrical solid,” in *Proc. IEEE Int. Ultrason. Symp. (IUS)*, Washington, DC, USA, 2017, pp. 1–4.
- [6] S. Biryukov, A. Sotnikov, and H. Schmidt, “SAW based tube rotation with wireless power transfer,” in *Proc. IEEE Int. Ultrason. Symp. (IUS)*, Kobe, Japan, 2018, pp. 1–3.
- [7] S.V. Biryukov, A.V. Sotnikov, H. Schmidt, Macroscopic disk rotation by means of surface acoustic waves, *IEEE Trans. UFFC* 69 (2022) 447–449.

- [8] D.F. Nelson, Electric, optic and acoustic interactions in dielectrics, Wiley, New York, 1979.
- [9] K.Y. Bliokh, Elastic spin and orbital angular momenta, *Phys. Rev. Lett.* 129 (2022) 204303.
- [10] H.F. Tiersten, On the nonlinear equations of thermo-electroelasticity, *Int. J. Eng. Sci.* 9 (1971) 587–604.
- [11] D.A. Berlincourt, D.R. Curran, H. Jaffe, Piezoelectric and piezomagnetic materials and their function in transducers, in: A Part (Ed.), *Physical Acoustics*, 1964, pp. 169–270.
- [12] B.A. Auld, *Acoustic fields and waves in solids*, 2nd ed., 1, Krieger Publishing, Malabar, FL, USA, 1990.
- [13] Ferroperm Piezoceramics, Full data matrix, <https://www.ferroperm-piezoceramics.com/materials/> (consulted May 05, 2023).
- [14] P. Yang, C. DiAntonio, G. R. Burns, D. J. Corelis, and D. F. Rae, Thermal properties of PZT95/5(1.8Nb) and PSZT ceramics, Sandia Report SAND2006-5437 (2006).
- [15] G. Feuillard, L.P. Tran-Huu-Hue, L. Tessier, C.E. Millar, M. Lethiecq, Study of mechanical and dielectric losses contribution to the surface-acoustic-wave attenuation in piezoelectric ceramics, *J. Appl. Phys.* 77 (1995) 3061–3066.
- [16] W. Ruile, “P-Matrix-Modelle von Oberflächenwellenbauelementen,” Dissertation, TU München, 1994 (in German).
- [17] W.N. Bodé, F. Lickert, P. Augustsson, H. Bruus, Determination of the complex-valued elastic moduli of polymers by electrical-impedance spectroscopy for ultrasound applications, *Phys. Rev. Appl.* 18 (2022) 064078.
- [18] N. Pérez, R.C. Carbonari, M.A.B. Andrade, F. Buiocchi, J.C. Adamowski, A FEM-based method to determine the complex material properties of piezoelectric disks, *Ultrasonics* 54 (2014) 1631–1641.
- [19] D. Berlincourt, “Piezoelectric crystals and ceramics,” in *Ultrasonics Transducer Materials*, ed. O. E. Mattiat, Plenum Press, New York (1971).
- [20] X.-H. Xu, J.-R. Chu, Preparation of a high-quality PZT thick film with performance comparable to those of bulk materials for applications in MEMS, *J. Micromech. Microeng.* 18 (2008) 065001-1–065001-7.
- [21] Q. Zou, H.E. Ruda, B.G. Yacobi, K. Saegusa, M. Farrell, Dielectric properties of lead zirconate titanate thin films deposited on metal foils, *Appl. Phys. Lett.* 77 (2000) 1038–1040.
- [22] J.B. Taylor, Torque on an ideal plasma, *Phys. Rev. Lett.* 91 (2003) 115002-1–3.
- [23] V.V. Krylov, Localized vibration modes propagating along edges of cylindrical and conical wedge-like structures, *J. Sound. Vib.* 227 (1999) 215–221.
- [24] C.-C. Yin and T.-H. Yu, “An ultrasonic motor driven by traveling cylindrical wedge waves,” in *Proc. IEEE Int. Ultrason. Symp. (IUS)*, Vancouver, Canada, 2006, pp. 156–159.
- [25] Z. Li, Z. Wang, P. Guo, L. Zhao, Q. Wang, A ball-type multi-DOF ultrasonic motor with three embedded traveling wave stators, *Sensors and Actuators A* 313 (2020), 112161-1- 12.
- [26] S.H. Jahantab, Y. Hojjat, B.G. Namin, M. Shirkosh, A novel spherical ultrasonic motor with wire stators and measuring torque and preload via a new method, *Sci. Rep.* 13 (2023) 11910-1-8.